Estimation of woodland canopy structure with terrestrial LiDAR: expanded methods

John L. Godlee

8th August 2021

1 Introduction

This chapter provides expanded field and analytical methods for the study of tree canopy structure in southern African woodlands, presented in brief in Chapter 5. The study aimed to understand the effects of tree species diversity and stand structure on tree canopy structural complexity, using terrestrial LiDAR. Firstly, I provide technical details on the field setup for the terrestrial LiDAR and the hemispherical photography used to validate terrestrial LiDAR canopy closure estimates. Secondly, I describe the processing chain used to extract canopy complexity metrics from the terrestrial LiDAR point clouds. Thirdly, I describe in further detail the behaviour and suitability of the different canopy complexity metrics and stand structural metrics used in the study.

2 Terrestrial LIDAR field setup

Within each 1 ha (100x100 m) square plot, nine 10 m diameter circular subplots were laid out in a grid, with 35 m between subplot centre points (Figure 1). These subplots constitute the basic sampling unit of the study. Within each subplot, a Leica HDS6100 phase-shift Terrestrial Laser Scanner (TLS) was used to capture woodland canopy structure. The number and position of scan locations within a subplot was determined by the arrangement and density of canopy material in the subplot. Scan positions were arranged to minimise shadows within the canopy, and to maximise canopy penetration. Between one and five scans were recorded per subplot, across all plots. Further information on the field setup of the TLS is presented in Table 1.

Five Leica 6" (15.24 cm) diameter planar tilt-and-turn cross-pattern reflective targets were used in each subplot to align scans (Figure 2). The five targets were located roughly in a quincunx pattern, with one target at the subplot centre and the remaining four targets arranged in a cross pattern around the edges of the subplot, ensuring that all scans could see all five targets. To facilitate alignment of scans among subplots, the location of each target in real space was recorded using a Leica VIVA GS10 GNSS (Global Navgation Satellite Systems) unit (Figure 3). The GNSS was set up in a Post-Processing Kinematic (PPK) configuration with a base-station located ~100 m from the edge of each 1 ha plot with an unobstructed view of the sky hemisphere where possible. The location of each target was measured for at least 4 minutes to minimise measurement error (Figure 4).

3 Hemispherical photography field setup

In order to validate TLS canopy closure estimates, at the centre of each subplot a single photograph was taken with a full-frame DSLR camera, equipped with a circular fisheye lens. Further information on the hemispherical photography setup is presented in Table 2.

The fisheye lens had an equisolid (equal area) projection, with a projection function given by:

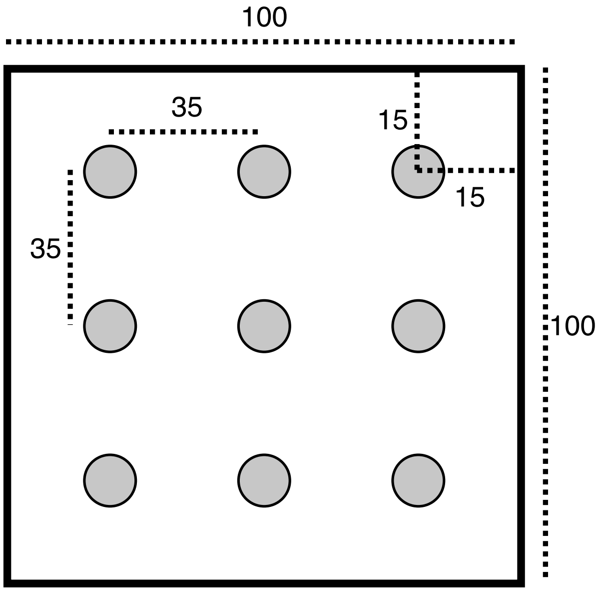

Figure 1: The layout of 10 m diameter subplots within each 1 ha plot. Each subplot is situated inside a 15 m buffer from the plot edge, with 35 m between subplot centres. Subplots are arranged in a 3x3 grid. All distances are in metres.

(a)

(b)

Figure 2: Example of a Leica 6" diameter reflective target, (a) in situ mounted on a length of threaded bar, and (b) showing the cross pattern face of the target.

Figure 3: A Leica VIVA GS10 GNSS unit in the field, showing the antenna atop an aluminium pole, attached to the base station on the ground, and the rover terminal in the hand of a research assistant.

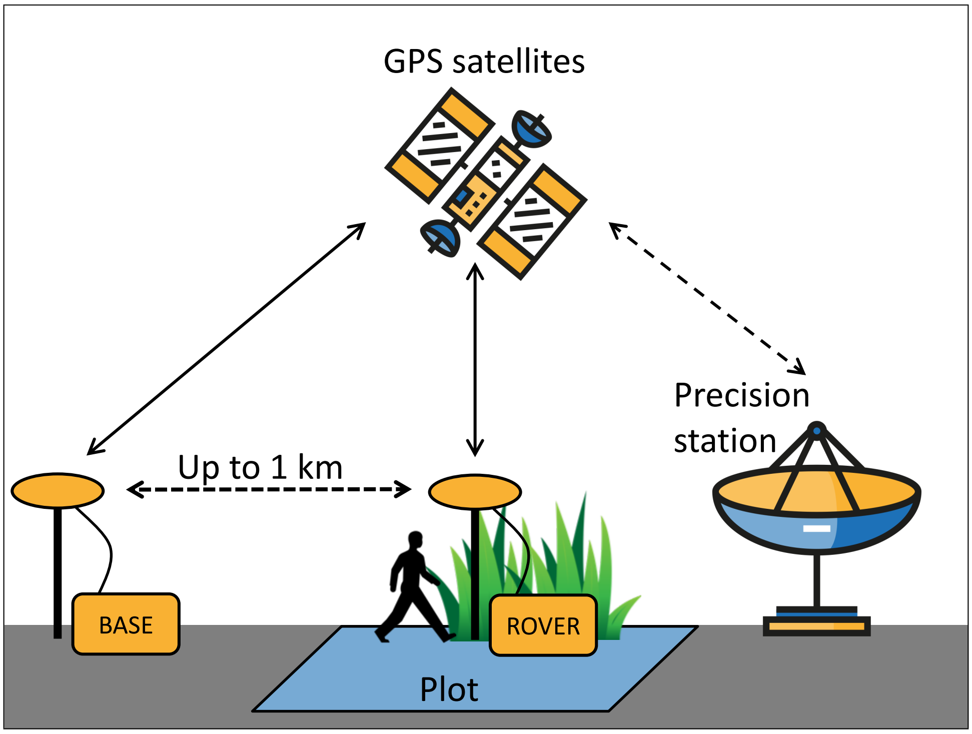

Figure 4: Schematic diagram of the GNSS PPK configuration used to precisely locate targets in real space. The base station is located in an area with a full unobstructed view of the sky hemisphere, up to ~1 km from the plot, and is left in the same location for the duration of the data collection, recording its location once per second. The rover is moved around inside the plot to record the location of each target, for >4 minutes at each target. The rover and the base station both utilise GPS and GLONASS satellites to record their position. After data collection, a two stage validation technique is used to improve the precision of the recorded positions, firstly using the base station, and secondly using the TrimbleRTX service which utilises highly precise distributed regional stations.

Table 1: Description of scan settings used for each scan.

Setting	Value
TLS model	Leica HDS6100
Wavelength	650-690 nm
Spot size at exit	3 mm
Beam divergence	0.22 mrad
Range	79 m @90%; 50 m @18% albedo
Azimuth range	0-360°
Zenith range	0-155°
Increment	0.018°
Point spacing over 25 m	7.9 mm
Pixels per line	20,000
Lines	10,000
Compressed file size	~800 MB
Duration of scan	6 minutes 44 seconds

$$R = 2f \sin\left(\frac{\theta}{2}\right) \tag{1}$$

Where R is the radial position of a point on the image, f is the focal length of the lens, and θ is the angle in radians of incident light on the lens. Equisolid lenses are preferred for hemispherical photography because they maintain an equal area for each pixel, i.e. a pixel projected through the lens has the same solid angle irrespective of the incident light angle, meaning that canopy closure estimations are not biased towards any part of the sky hemisphere (Herbert, 1987).

Photographs were taken facing directly to zenith using a camera-mounted spirit level, with the top of the camera body facing magnetic north, at a height of 1.3 m or above understorey vegetation, whichever was higher. Photographs were captured under uniform light conditions as much as possible, either under overcast skies or early in the day before direct sunlight could be seen on the photograph, to minimise lens flare, which can preclude accurate differentiation of plant material and sky, and 'blooming', a phenomenon where light 'bleeds' into dark areas of the image in highly contrasting light conditions (Frazer et al., 2001).

ImageJ (Fiji version 2.1.0/1.53c) was used to binarize hemispherical photographs, to separate plant material from sky (Schneider et al., 2012). Images were binarised using the Huang algorithm (Huang & Wang, 1995) using only the blue channel of the image, under the assumption that plant material reflects little blue light, while the sky reflects much more (Brusa & Bunker, 2014). Images were saved as PNG files at the original pixel resolution, with a circular image of 4016x4016 pixels.

4 Terrestrial LiDAR processing

4.1 Scan alignment and registration

Point clouds within a subplot were aligned using the reflective targets as anchor points. Point cloud alignment was conducted in Leica Cyclone (version 9.1) (Leica Camera AG, 2009). Reflective targets were manually located within each point cloud, then the precise centre of each target was identified automatically by Cyclone. Anchor points were discarded if they had

Table 2: Description of camera settings used for hemispherical photographs. Note that shutter speed and ISO are deliberately variable within sensible thresholds to allow adjustments for ambient light conditions.

Setting	Value
Camera model	Nikon D750
Lens model	Sigma 8 mm f/3.5 EX DG Circular Fisheye
Pixel pitch	5.95 µm
Sensor resolution	24.3 MP
Shutter speed	>1/60s
Aperture	5-7
ISO	100-200
Exposure compensation	-0.7 (Brusa & Bunker, 2014)
Focus	∞ (Hu & Zhu, 2009; Frazer et al., 2001)
Image size	Large Fine JPEG - circular image 4016x4016 px
Orientation	Landscape

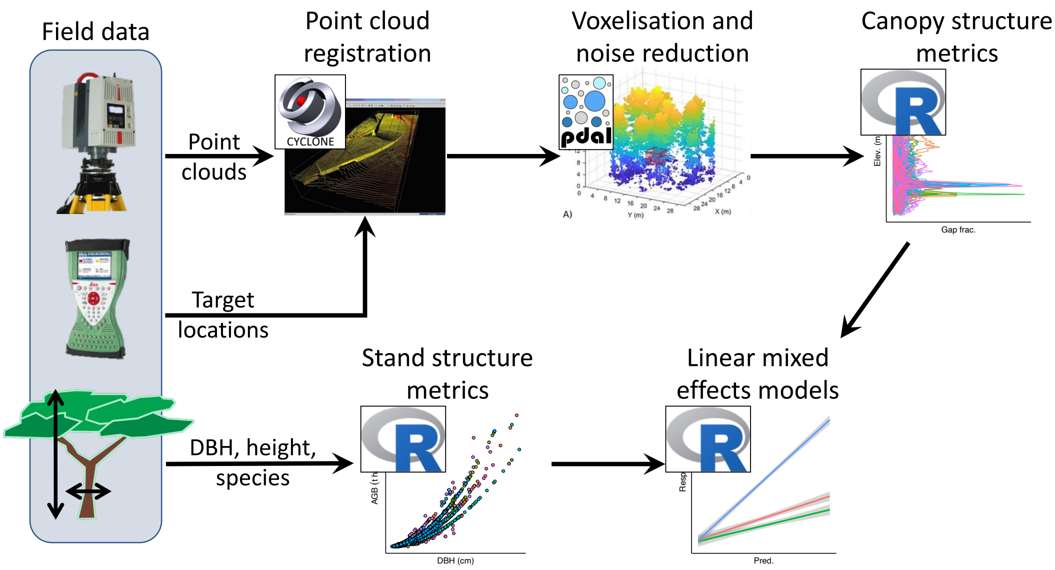

Figure 5: Schematic diagram summarising the data processing and analysis workflow for the TLS data. Processing steps are labelled according to the principal software used during that step.

a location uncertainty of >3 cm. After alignment, subplot point clouds were exported from Cyclone as PTX files for further processing.

GNSS target locations were used to register point clouds in real space. The TrimbleRTX GNSS post-processing service was used to improve the precision of target locations recorded with GNSS, using distributed regional stations to validate the rover and base station GNSS measurements (Chen et al., 2011). Following point cloud registration, subplot point clouds were combined to a plot-level point cloud.

PTX files were converted to compressed LAZ files using PDAL (PDAL Contributors, 2018), to reduce file size and speed up further processing. Code 1 contains the code used to transform PTX to LAZ.

```
# Get file name without extension
noext=${1%.ptx}

# Find the PTX scan array dimension header material
lines=$(grep -E -n '^.{1,10}$' $1 |
  cut -f1 -d: |
  awk 'NR%2!=0' |
  tr '\n' ' ' |
  sed 's/^[0-9]\s//g')

# Split PTX file into individual scans
csplit -f "$noext" -b "_%d.ptx" $1 $lines

$ Find split files
ptxsplit=$(find . -type f -regex ".*/${noext}_[0-9].ptx")

# For each file:
for j in ${ptxsplit} ; do
  jnoext="${j%.ptx}"
  matrix=$(head -n 10 $j | tail -4 | sed -r 's/0\s+?$/0.0/g' | dos2unix)
  pdal pipeline ptx_laz.json --readers.text.filename=$j \
    --filters.transformation.matrix="${matrix}" \
    --writers.las.filename=${jnoext}.laz
done

# List LAZ files
lazsplit=$(find . -type f -regex ".*/${noext}_[0-9].laz")

# Merge LAZ files
pdal merge ${lazsplit} ${noext}.laz
```

Code 1: The processing chain used to convert Leica Cyclone PTX files to LAZ files, using PDAL, POSIX shell scripting, and common UNIX utilities. The `ptx_laz.json` JSON pipeline is shown in Code 2.

```
[
  {
    "type" : "readers.text",
    "filename" : "input.txt",
        "header" : "X Y Z I",
        "skip" : 10
  },
   {
        "type" : "filters.transformation",
        "matrix" : "0 -1  0  1  1  0  0  2  0  0  1  3  0  0  0  1"
    },
    {
        "type" : "writers.las",
        "compression" : "true",
        "minor_version" : "2",
        "dataformat_id" : "0",
        "forward" : "all",
        "filename" : "output.laz"
    }
]
```

Code 2: The JSON pipeline used in Code 1 to convert PTX files to LAZ files, and applying a rotation matrix.

4.2 Voxelisation

Point clouds were voxelised to different voxel sizes depending on the application of the data. 5 cm^3 cubic voxels were used for subplot height profile estimation, while 50 cm^3 voxels were used for whole plot canopy rugosity. Variation in voxel size reflects the spatial scale of each analysis, and is bounded by the beam divergence of the scanner over longer distances (Grau et al., 2017). Choosing voxels that are too small can result in pock-marked representations of surfaces that are especially problematic when calculating larger scale canopy structure metrics such as canopy top roughness, while voxels that are too large can result in an over-estimation of plant volume when estimating canopy foliage density at the subplot scale, especially when foliage is clumped (Seidel et al., 2012; Cifuentes et al., 2014). Voxels were classified as 'filled' if they intersected one or more points.

4.3 Noise reduction

Outlier detection and noise reduction of point clouds was conducted in PDAL, using the "statistical method" (sensu Rusu et al. 2008) of `filters.outlier`, with $k = 8$ (mean number of neighbours), and $m = 1.96$ (outlier distance threshold multiplier, here approximating a 95% confidence interval):

$$\begin{aligned}
\overline{\mu} &= \frac{1}{N}\sum_{i=1}^{N}\mu_i \\
\sigma &= \sqrt{\frac{1}{N-1}\sum_{i=1}^{N}(\mu_i - \overline{\mu})^2} \\
t &= \mu + m\sigma \\
\text{with } outlier_i &= \begin{cases} \text{true}, & \text{if } \mu_i >= t \\ \text{false}, & \text{otherwise} \end{cases}
\end{aligned} \tag{2}$$

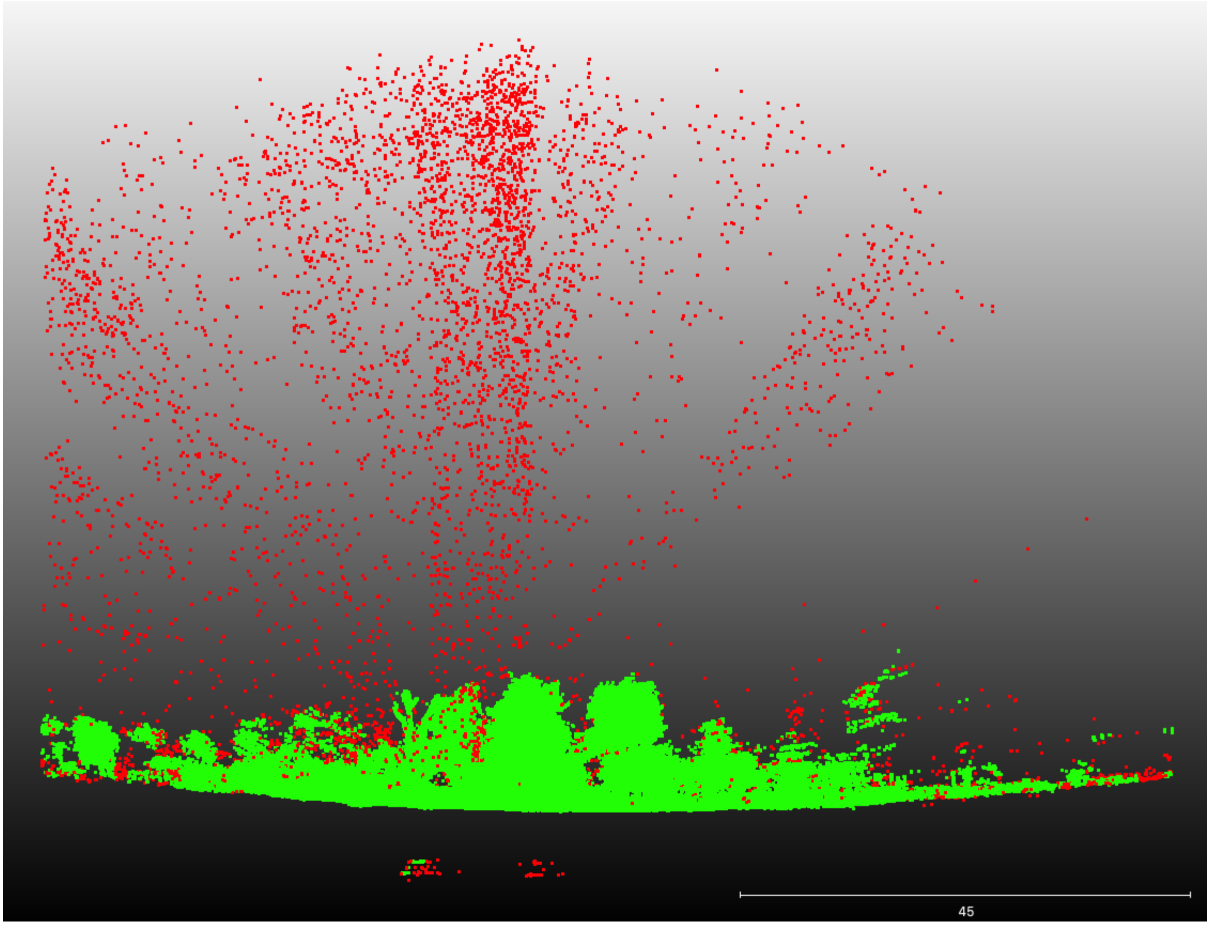

Figure 6: A 2 m deep cross section of a subplot point cloud showing the efficacy of the noise reduction and voxelisation process. Red points are excluded by the process, while green points are preserved for further analysis.

where μ_i is the mean distance from point i to all k nearest neighbour points, N is the number of points in the scene, $\overline{\mu}$ is the mean distance to nearest neighbour points, σ is the standard deviation of these mean distances, t is the threshold distance used to define an outlier and $outlier_i$ is the condition of a point in the scene being identified as an outlier.

4.4 Foliage density profiles

To calculate subplot foliage density profiles, the 5 cm^3 voxelised point cloud was first cropped to a 10 m diameter cylinder of infinite height. Ground points were identified using `filters.pmf` (Progressive Morphological Filter - PMF) in PDAL (sensu Zhang et al. 2003), and the height above ground of all points was calculated using `filters.hag_nn` (Nearest Neighbour) in PDAL. Points below ground level and above the 99.9th percentile of height were excluded from further analyses. Height profile points were exported to XYZ coordinates then imported into R for further processing.

In R, foliage density was calculated in 5 cm layers as the proportion of filled 5 cm^3 voxels. A loess model with a span of 0.1 was fitted to the foliage density values in each layer to estimate the foliage density profile (Figure 7). The foliage density profile was further filtered to only tree canopy material, by discarding all points below the first local minima in the foliage density profile above 1.3 m, using a rolling window of 50 cm.

Multiple statistics were extracted from the foliage density profile for use in statistical analyses.

Total canopy foliage density was calculated as the area under the curve of the canopy foliage density profile, using trapezoid estimation. The Effective Number of Layers (ENL) in the foliage density profile was used to estimate canopy structural complexity, using the true-numbers equivalent of the Shannon diversity index on the foliage density of 50 cm layers (sensu (Ehbrecht et al., 2016)):

$$\mathrm{ENL} = \exp\Big(- \sum_{i=1}^{N} p_i \mathrm{ln} p_i \Big) \tag{3}$$

Where N is the number of 50 cm bins in the height profile, and p_i is the proportion of filled voxels in layer i (foliage density). While Ehbrecht et al. (2016) used 1 m layers, their study was conducted in temperate deciduous forest where the maximum height of the sampled forest stands was 40 m, whereas the maximum canopy height in this study was only 22 m. Both Ehbrecht et al. (2016) and Montes et al. (2004) assert that layer thickness is largely arbitrary, but should be determined with respect to the variability within the canopy, thus in the sparse and highly variable savanna tree canopies measured in this study, narrower layers were chosen.

To describe the uniformity of the foliage density distribution through the canopy, a linear model of foliage density with height was fitted. Under a completely even distribution of foliage material through the canopy, the standard error of the linear model tends to zero, while clumping causes deviations from this uniform distribution and increases the standard error.

4.5 Canopy closure

Subplot canopy closure, i.e. the proportion of the sky hemisphere occluded by plant material, a.k.a. gap fraction or site factor (Jennings, 1999), was measured by simulating a hemispherical image at the centre of the subplot using the point cloud data from all scans per subplot. The point cloud was first cropped to a 20 m diameter cylinder around the subplot centre using PDAL. Points below 1.3 m and within a 50 cm sphere around the subplot centre at 1.3 m height were discarded, to prevent the simulated hemispherical image being occluded by understorey vegetation. POV-Ray was used to simulate the hemispherical image using ray-tracing (Persistence of Vision Pty. Ltd., 2004). Filled voxels were represented in POV-Ray as non-reflective black cubes filling the 5 cm^3 voxel volume, with a white uniform sky box and no light source. POV-Ray produced an image with identical qualities to that of the real hemispherical photograph, using a fisheye lens with an equisolid projection and a view angle of 180°, located at the subplot centre at 1.3 m above the ground, with the top of the camera facing magnetic north and the camera facing directly to zenith, producing a circular image of 4016x4016 pixels.

Hemiphot (ter Steege, 2018) was used to estimate closure from both the hemispherical photographs and the TLS POV-Ray simulation. Hemiphot calculates canopy closure in 90 evenly sized concentric rings. To obtain the total closure of a circular image:

$$C_\alpha = 1 - G_{\mathrm{tot}} = \sum_{\alpha=0.5}^{\alpha=89.5} (G_\alpha A_\alpha / A_{\mathrm{tot}}) \tag{4}$$

Where G_α is the fraction of unfilled pixels in ring α, A_α is the sky area of the ring segment, and A_{tot} is the total sky area of the hemisphere.

Canopy closure estimates from the TLS were validated using estimates from hemispherical photography. A Pearson's correlation analysis showed that both methods were highly correlated ($r(195)=0.89$, $p<0.001$). TLS estimates of closure were almost exclusively higher than hemispherical photography estimates, except in a few subplots with particularly low canopy closure. At higher canopy closure the over-estimation of canopy closure by TLS was larger (Figure 8). This

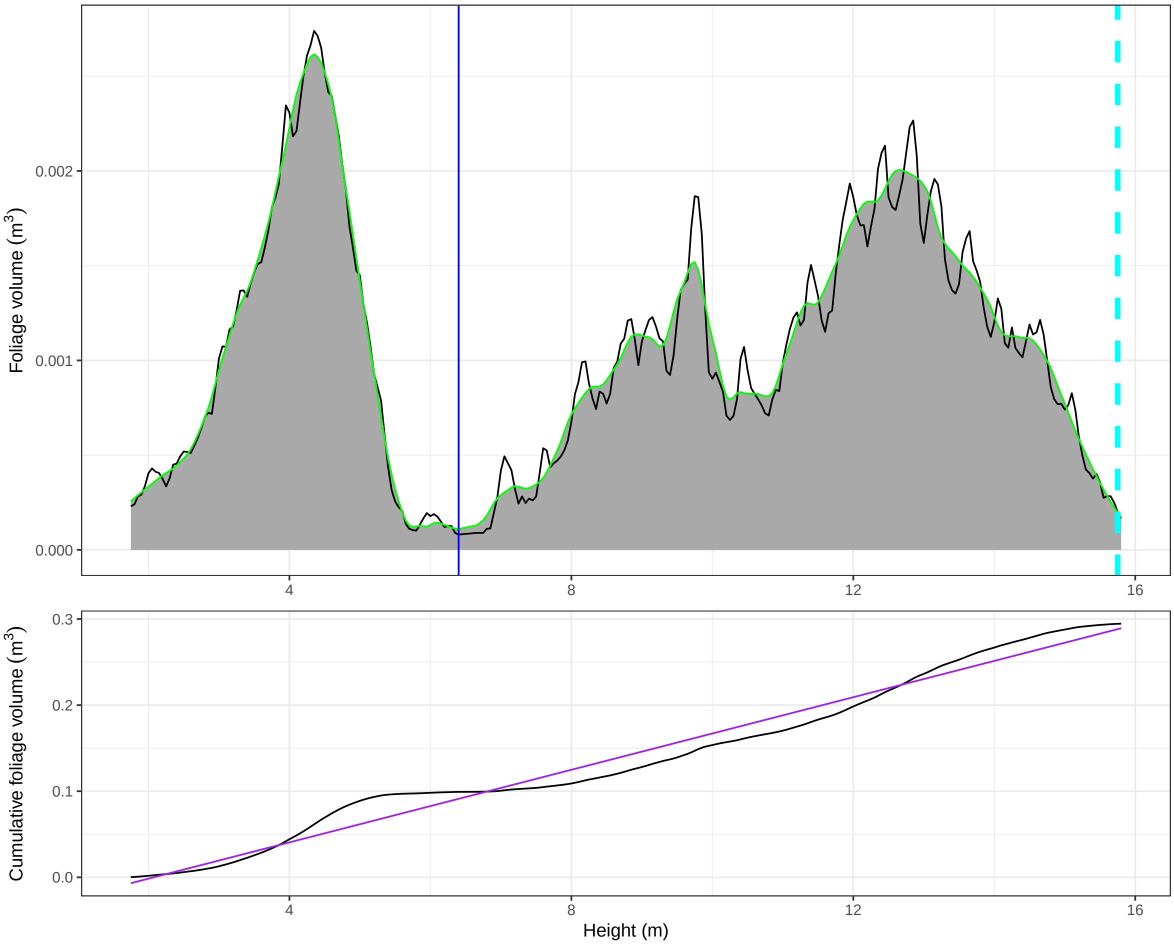

Figure 7: Subplot foliage volume height profile (top) and cumulative foliage volume profile (bottom) for a subplot in Bicuar National Park, Angola, to illustrate some of the canopy structure metrics extracted from each height profile. Starting with the top panel: the blue solid line represents the first local minima above 1.3 m, used to define the base of the tree canopy. The dashed cyan line shows the 99.9th percentile of canopy height, used here as a measure of canopy top height across the subplot and in plot-level canopy surface modelling. The black trace shows the foliage density height profile, and the green trace shows the loess model fitted to the data, with the area under the canopy shaded grey. The bottom panel: the black trace shows the cumulative foliage volume through the canopy, taken from the loess fit in the top panel. The purple line shows the line of best fit of a linear model through this data. Not illustrated is the Effective Number of Layers (ENL) metric.

finding is in agreement with previous studies which have found that that the magnitude of TLS canopy closure over-estimation depends on gap size distribution, where a site with greater canopy cover and a gap fraction dominated by small within crown gaps will have a larger over-estimate than a more open site with a gap fraction dominated by large between crown gaps (Seidel et al., 2012). A linear mixed model which accounted for the nested sampling of subplots within plots was used to identify if sites differed significantly in their relationship between hemispherical photography and TLS estimates of canopy closure. There was no significant difference in model fixed effect slope between plots in Bicuar National Park, Angola, and those in Mtarure, Tanzania ($\beta(173)$=0.13±0.0098, p=0.18).

4.6 Whole plot canopy metrics

The canopy height of each 1 ha plot was estimated using unified point clouds from all subplots. The unified point cloud was voxelised to 10 cm^3, and the 99th percentile of height from each 10 cm^2 column was taken as the canopy height. Maximum height was not used as this occasionally constituted a severe outlier which skewed further canopy surface model smoothing. The point cloud was then cropped to the plot boundaries, located using PPK GNSS similar to the TLS targets. A pit-filling algorithm described in Khosravipour et al. (2014) was used to smooth the canopy surface model, at a resolution of 50 cm, by removing gaps within trees caused by incomplete penetration of the LiDAR beam (Figure 10).

Mean canopy height across the plot and the coefficient of variation of canopy height were extracted from the canopy surface model for use in statistical analyses. The coefficient of variation of canopy height describes canopy structural diversity. Canopy rugosity (R_c) was also calculated to describe structural complexity across the entire canopy profile, rather than just the canopy surface, sensu Hardiman et al. (2011). R_c first calculates the standard deviation of foliage density in 50 cm^2 columns across the plot (σG_z), then calculates the standard deviation of those standard deviations:

$$R_c = \sigma(\sigma G_z)_x \tag{5}$$

Where G_z is the vertical height axis z, x is the horizontal axis, and σ is the standard deviation. Finally, plot-level canopy closure was calculated as the mean of subplot TLS canopy closure estimates.

5 Stand structure metrics

5.1 Spatial mingling of species

The spatial mingling index (M_i) is a spatially explicit estimate of the degree to which species are spatially mixed within a plot. Here, M was calculated at the plot level as the mean of M_i according to von Gadow & Hui (2002), with the adjustment for potential neighbourhood species pool suggested by Hui et al. (2011):

$$\begin{aligned} M &= \overline{M_i} \\ M_i &= \frac{S_i}{n_{\max}} \frac{1}{k} \sum_{j=1}^{k} v_j \\ \text{with } v_j &= \begin{cases} 0, & \text{neighbour } j \text{ same species as reference } i \\ 1, & \text{otherwise} \end{cases} \end{aligned} \tag{6}$$

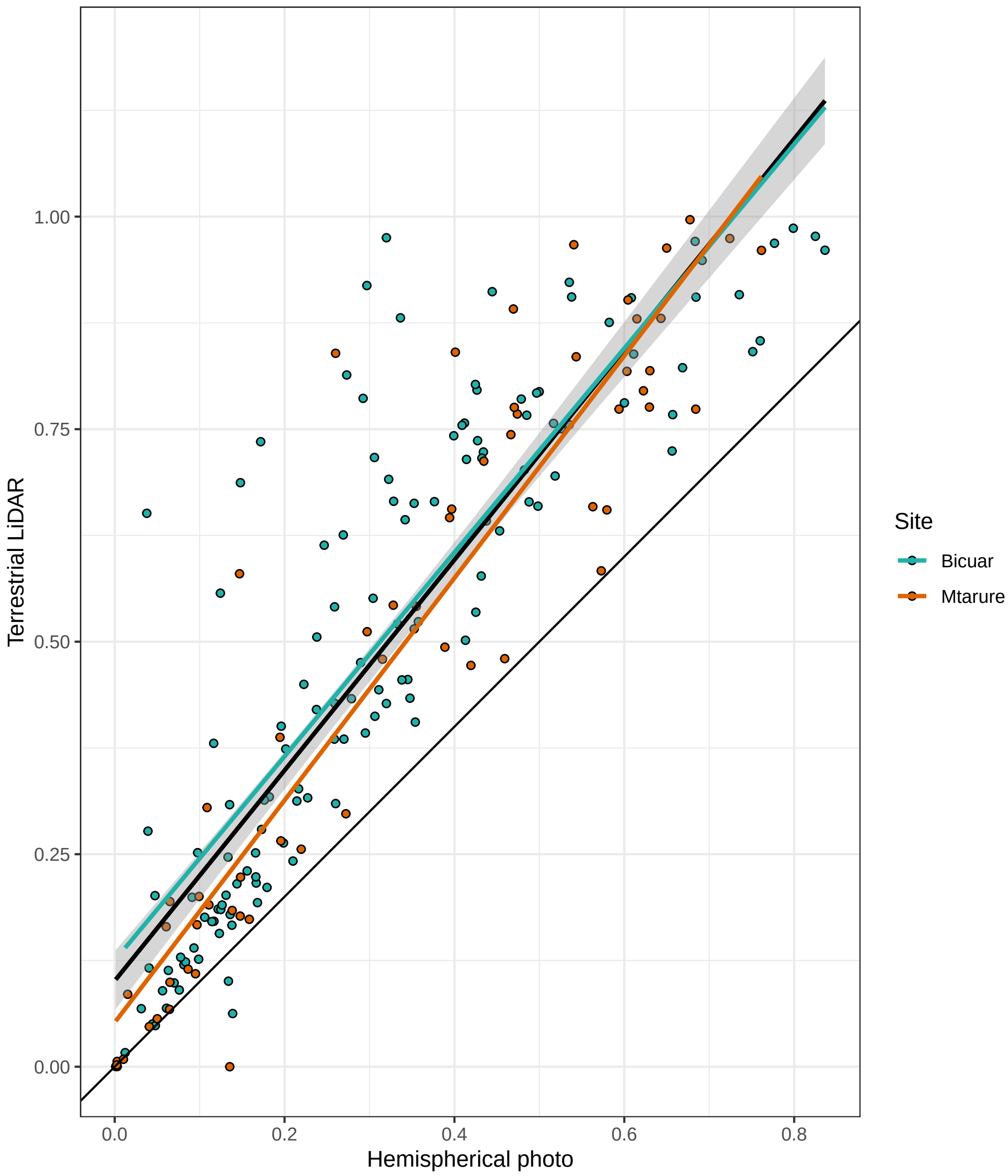

Figure 8: Comparison of canopy closure estimation from TLS and hemispherical photography. The thick black line of best fit is a linear model of all points ±1 standard error, while the coloured lines are site specific linear models. The thin black line shows the 1:1 fit.

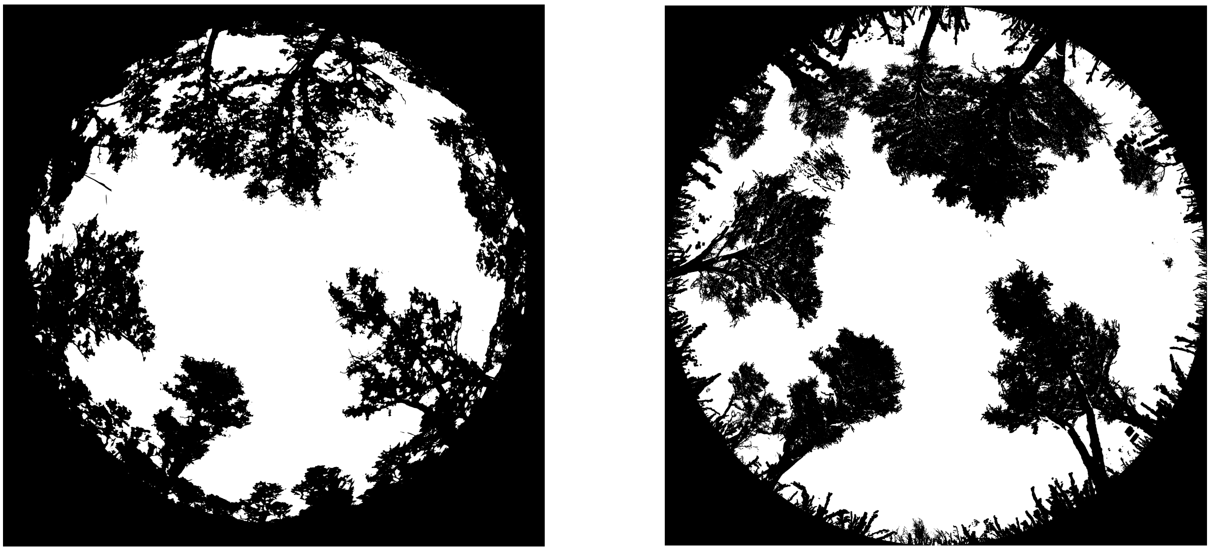

(a) (b)

Figure 9: Comparison of hemispherical images for a subplot in Bicuar National Park, Angola. (a) A hemispherical photograph, and (b) a multi-scan point cloud modelled as cubic voxels with POV-Ray. The hemispherical photograph (left) shows some blooming, especially in the tree on the bottom right of the image, where light is seen 'bleeding' through the darker canopy material, causing an under-estimation in canopy closure.

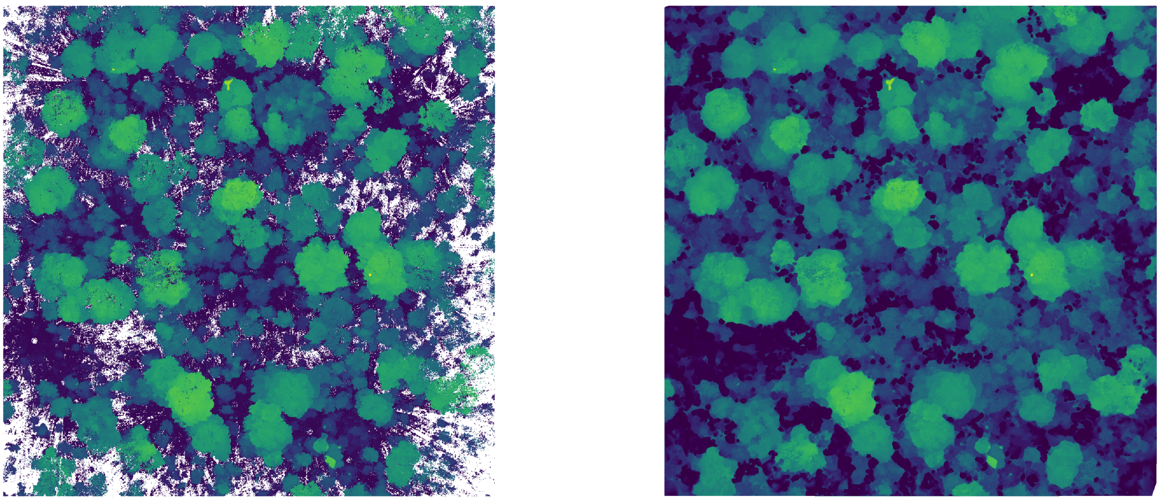

(a) (b)

Figure 10: Top-down view of a 1 ha plot in Bicuar National Park. (a) The point cloud after voxelisation, noise reduction, and taking the 99th percentile of stem height in each 5 cm vertical bin. (b) The same point cloud after pit filling to generate a smooth canopy height profile. Points are coloured according to point height from the ground.

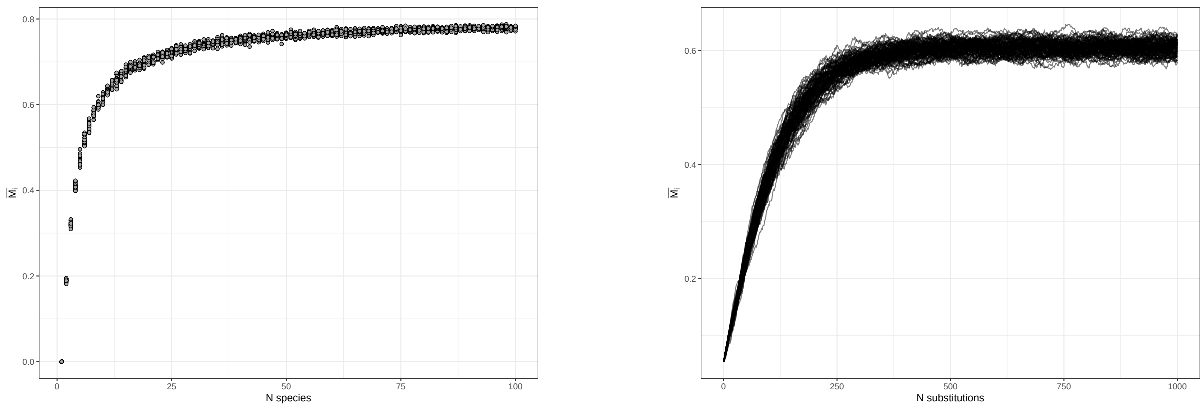

(a) (b)

Figure 11: The behaviour of M_i with increasing number of species (a), and increasing spatial mixing of species (b). The left panel was generated by randomly assigning different numbers of species, in equal proportions, to an evenly spaced grid of individuals. 20 replicates were conducted for each number of species. The right panel was generated by randomly swapping pairs of individuals in a plot with 9 species arranged in mono-specific square blocks in an evenly spaced grid. Each line shows a single replicate, where individuals were swapped in an additive fashion, with 100 total.

Where k is the number of nearest neighbours considered for each reference tree, S_i is the number of species found among the k nearest neighbours of tree i, $n_{\max}$ is the potential number of species in the neighbourhood, i.e. $k + 1$, and N is the total number of trees in the plot. The conventional value of $k = 4$ was used here (von Gadow & Hui, 2002; Hui & Albert, 2004; Hui et al., 2007). The value of M_i increases with greater mixing of species, and all else being equal will increase with number of species within the plot (Figure 11).

5.2 Spatial clustering of stems

The winkelmass (W) was calculated to estimate the degree of spatial uniformity in stem spatial distribution. Here, W was calculated at the plot level as the mean of W_i) according to von Gadow & Hui (2002):

$$\begin{aligned} W &= \overline{W_i} \\ W_i &= \frac{1}{k}\sum_{j=1}^{k} v_j \\ \text{with } v_j &= \begin{cases} 0, & \alpha_j \leq \alpha_0 \\ 1, & \text{otherwise} \end{cases} \end{aligned} \tag{7}$$

Where k is the number of neighbours considered, here using the conventional value of $k = 4$, α_j is the angle between consecutive neighbours and α_0 is the critical angle, where $\alpha_0 = 360/k$. Figure 12 demonstrates how the value of W_i varies according to spatial distribution of neighbours. The value of the winkelmass increases with increasing spatial clumping (decreasing spatial regularity) of individuals (Figure 13), and in a plot with random tree distribution will increase as more neighbours are considered (Figure 14).

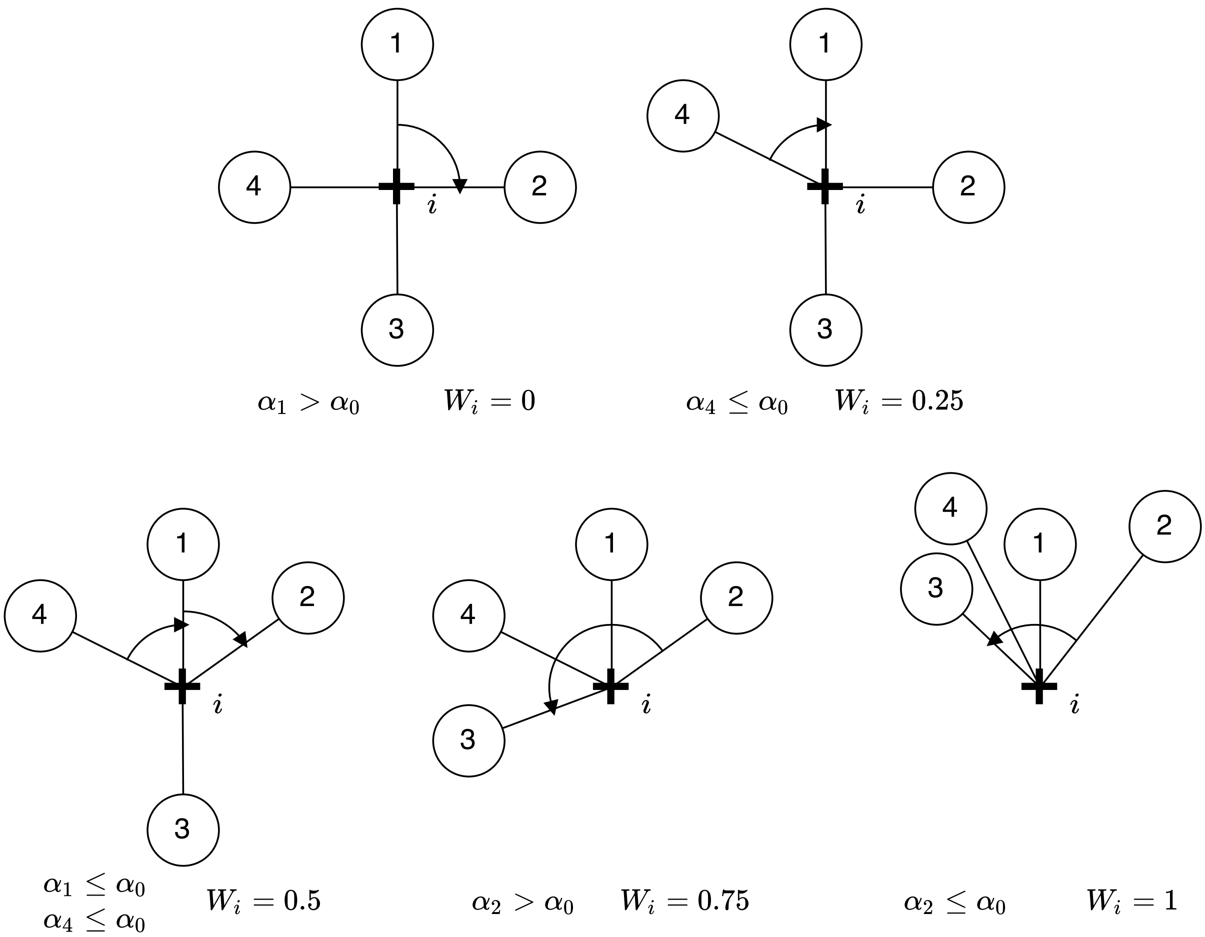

Figure 12: Possible values of W_i at a sample point i, denoted by a cross. Neighbours are represented as circles numbered sequentially from 1 to 4, where $k = 4$. The angles of arrows in each example are given below, along with the winkelmass for that example.

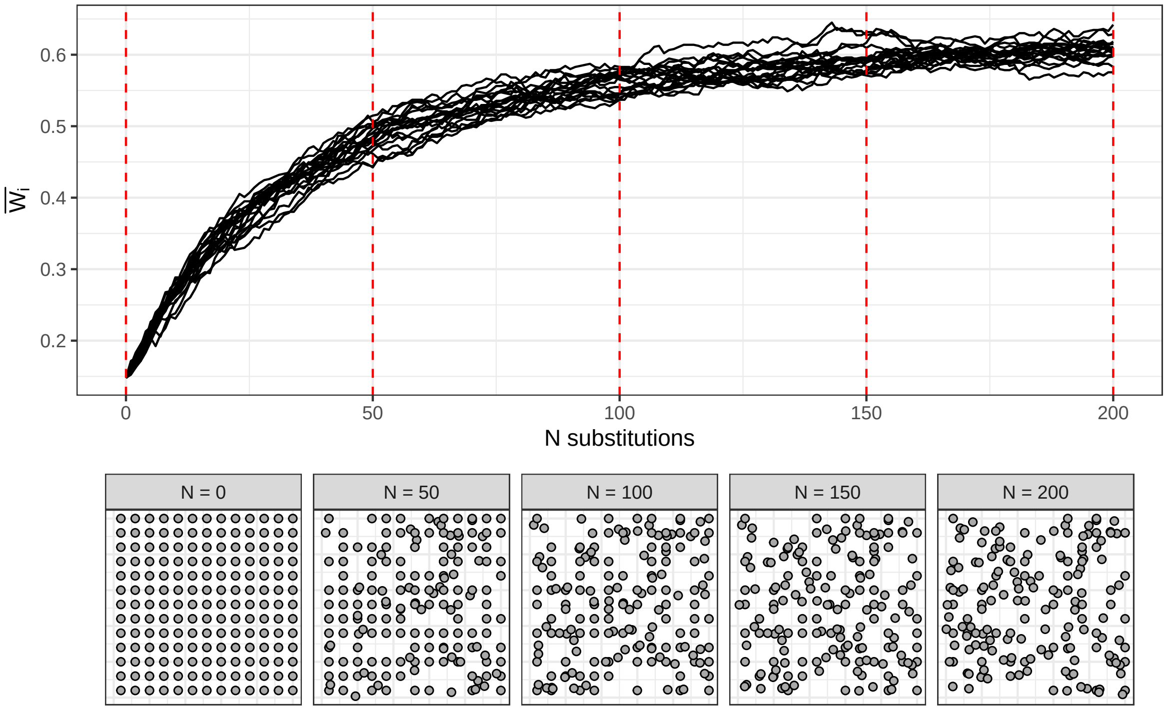

Figure 13: Variation in winkelmass with increasing spatial irregularity of individuals. The top panel shows variation of winkelmass in 20 plots as individuals are sequentially moved to a random location within the plot. Red dotted lines correspond to the panels below which show the spatial distribution of individuals after a given number of random individual movements.

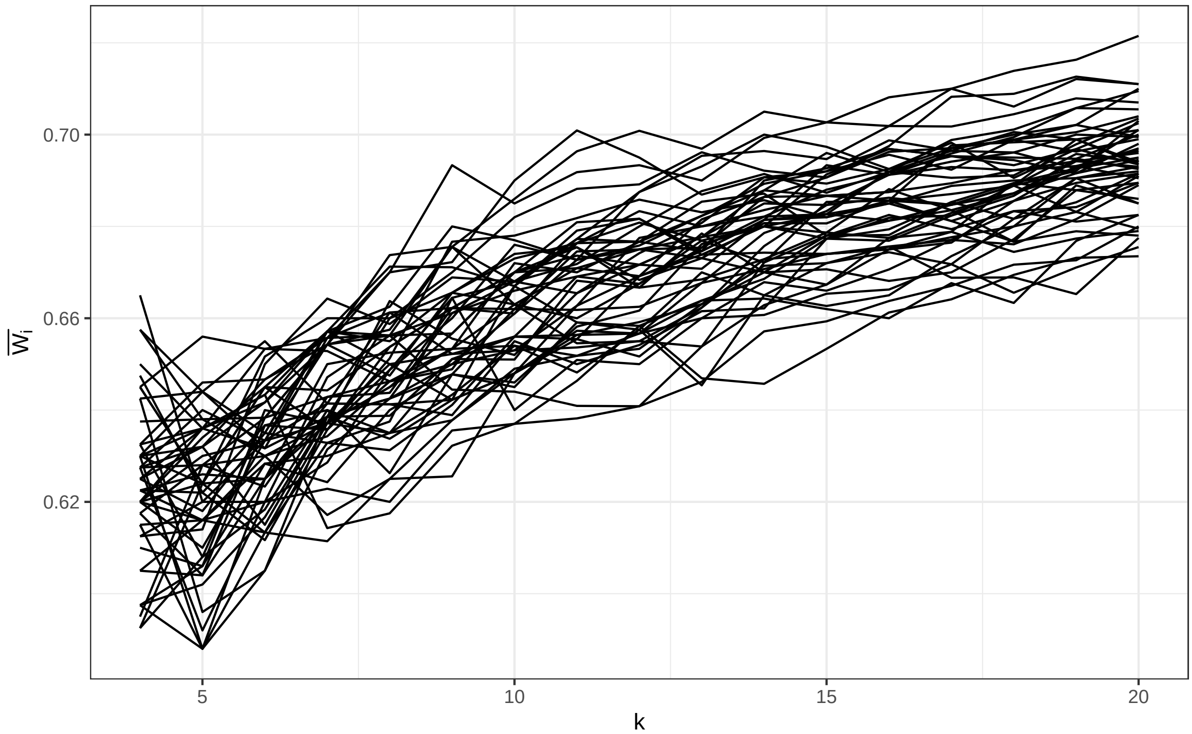

Figure 14: Variation in winkelmass with increasing number of neighbours k considered in the calculation. 50 replicate plots were used, each with 100 individuals randomly distributed in space.

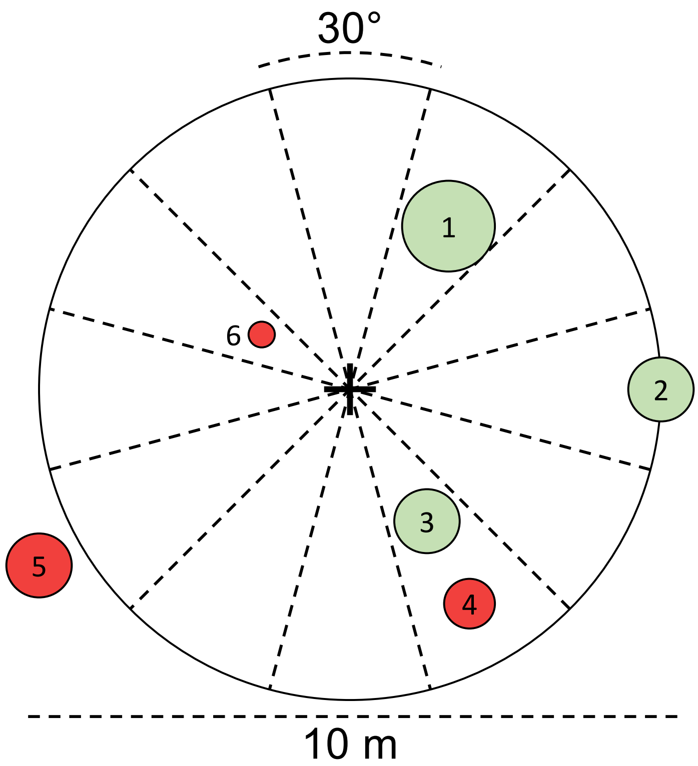

Figure 15: Schematic diagram demonstrating use of the Iterative Hegyi Index to assess crowding within each subplot. The 10 metre diameter subplot is divided into 12 equally sized sectors. Within each sector, the nearest stem of sufficient size (>5 cm diameter) to the subplot centre is recorded (e.g. 1). All stems with any canopy material inside the subplot are valid (e.g. 2). Stem 4 is not valid as it is behind stem 3. Stem 5 is invalid as all its canopy is outside the subplot. Stem 6 is too small to be recorded.

5.3 Subplot canopy crowding

An adapted version of the Iterative Hegyi Index (H_i) was used to estimate tree spatial structure in subplots (Hegyi, 1974). The adapted formula used here allows the index to be based on a point rather than a focal tree, transforming it from a tree-centric competition index to a point-centric crowding index:

$$H_i = log \sum_{j=1}^{n} (\frac{1}{L_{ij}} D_j) \quad (8)$$

Where n is the number of stems with canopy material within the subplot, D_j is the stem diameter of stem j and L_{ij} is the distance of stem j from the subplot centre i. H_i uses an iterative method for choosing active canopy occupants at the subplot centre, where the nearest individual to the subplot centre from each of 12 equally sized sectors is classified as the active stem (Figure 15). H_i was preferred over stem density to describe stem crowding in subplots because it is sensitive to how close a stem is to the subplot centre, which will affect canopy closure even if the number of stems in the subplot remains the same.

References

Brusa, A. & D. E. Bunker (2014). ‘Increasing the precision of canopy closure estimates from hemispherical photography: Blue channel analysis and under-exposure’. In: *Agricultural and Forest Meteorology* 195-196, pp. 102–107. DOI: 10.1016/j.agrformet.2014.05.001.

Chen, X., T. Allison, W. Cao, K. Ferguson, S. Gr unig, V. Gomez, A. Kipka, J. K ohler, H. Landau, R. Leandro et al. (Sept. 2011). *Trimble RTX, an innovative new approach for network RTK*. Tech. rep. Portland OR, USA: International Technical Meeting of the Satellite Division of the Institute of Navigation, ION GNSS, pp. 2214–2219.

Cifuentes, R., D. V. der Zande, J. Farifteh, C. Salas & P. Coppin (2014). ‘Effects of voxel size and sampling setup on the estimation of forest canopy gap fraction from terrestrial laser scanning data’. In: *Agricultural and Forest Meteorology* 194, pp. 230–240. DOI: 10.1016/j.agrformet.2014.04.013.

Ehbrecht, M., P. Schall, J. Juchheim, C. Ammer & D. Seidel (2016). ‘Effective number of layers: A new measure for quantifying three-dimensional stand structure based on sampling with terrestrial LiDAR’. In: *Forest Ecology and Management* 380, pp. 212–223. DOI: 10.1016/j.foreco.2016.09.003.

Frazer, G. W., R. A. Fournier, J. Trofymow & R. J. Hall (2001). ‘A comparison of digital and film fisheye photography for analysis of forest canopy structure and gap light transmission’. In: *Agricultural and Forest Meteorology* 109.4, pp. 249–263. DOI: 10.1016/s0168-1923(01)00274-x.

Grau, E., S. Durrieu, R. Fournier, J.-P. Gastellu-Etchegorry & T. Yin (2017). ‘Estimation of 3D vegetation density with Terrestrial Laser Scanning data using voxels. A sensitivity analysis of influencing parameters’. In: *Remote Sensing of Environment* 191, pp. 373–388. DOI: 10.1016/j.rse.2017.01.032.

Hardiman, B. S., G. Bohrer, C. M. Gough, C. S. Vogel & P. S. Curtis (2011). ‘The role of canopy structural complexity in wood net primary production of a maturing northern deciduous forest’. In: *Ecology* 92.9, pp. 1818–1827. DOI: 10.1890/10-2192.1.

Hegyi, F. (1974). ‘A simulation model for managing jack-pine stands’. In: *Royal College of Forestry, editor*. Stockholm, Sweden: Royal College of Forestry, pp. 74–90.

Herbert, T. J. (1987). ‘Area projections of fisheye photographic lenses’. In: *Agricultural and Forest Meteorology* 39.2-3, pp. 215–223. DOI: 10.1016/0168-1923(87)90039-6.

Hu, L. & J. Zhu (2009). ‘Determination of the tridimensional shape of canopy gaps using two hemispherical photographs’. In: *Agricultural and Forest Meteorology* 149.5, pp. 862–872. DOI: 10.1016/j.agrformet.2008.11.008.

Huang, L. & M. J. Wang (1995). ‘Image thresholding by minimizing the measures of fuzziness’. In: *Pattern Recognition* 28.1, pp. 41–51. DOI: 0031-3203/95.

Hui, G. & M. Albert (2004). ‘Stichprobensimulationen zur Schätzung nachbarschaftsbezogener Strukturparameter in Waldbeständen [Simulation studies for estimating neighborhood-based structural parameters in forest stands]’. In: *Allgemeine Forst und Jagdzeitung* 175, pp. 10–11.

Hui, G., K. von Gadow, Y. Hu & H. Xu (2007). *Structure-based forest management*. Beijing, China: China Forestry Publishing House.

Hui, G., X. Zhao, Z. Zhao & K. von Gadow (2011). ‘Evaluating tree species spatial diversity based on neighbourhood relationships’. In: *Forest Science* 57.4, pp. 292–300. DOI: 10.1093/forestscience/57.4.292.

Jennings, S. (1999). ‘Assessing forest canopies and understorey illumination: canopy closure, canopy cover and other measures’. In: *Forestry* 72.1, pp. 59–74. DOI: 10.1093/forestry/72.1.59.

Khosravipour, A., A. K. Skidmore, M. Isenburg, T. Wang & Y. A. Hussin (2014). ‘Generating Pit-free Canopy Height Models from Airborne LiDAR’. In: *Photogrammetric Engineering & Remote Sensing* 80.9, pp. 863–872. DOI: 10.14358/pers.80.9.863.

Leica Camera AG (2009). *Leica Cyclone*. Version 9.1.

Montes, F., I. Cañellas, M. del Río, R. Calama & G. Montero (2004). 'The effects of thinning on the structural diversity of coppice forests'. In: *Annals of Forest Science* 61.8, pp. 771–779. DOI: 10.1051/forest:2004074.

PDAL Contributors (2018). *PDAL Point Data Abstraction Library*. DOI: 10.5281/zenodo.2556738.

Persistence of Vision Pty. Ltd. (2004). *Persistence of Vision Raytracer (Version 3.7)*. [Computer software].

Rusu, R. B., Z. C. Marton, N. Blodow, M. Dolha & M. Beetz (2008). 'Towards 3D Point cloud based object maps for household environments'. In: *Robotics and Autonomous Systems* 56.11, pp. 927–941. DOI: 10.1016/j.robot.2008.08.005.

Schneider, C. A., W. S. Rasband & K. W. Eliceiri (2012). 'NIH Image to ImageJ: 25 years of image analysis'. In: *Nature Methods* 9.7, pp. 671–675. DOI: 10.1038/nmeth.2089.

Seidel, D., S. Fleck & C. Leuschner (2012). 'Analyzing forest canopies with ground-based laser scanning: A comparison with hemispherical photography'. In: *Agricultural and Forest Meteorology* 154-155, pp. 1–8. DOI: 10.1016/j.agrformet.2011.10.006.

ter Steege, H. (2018). *Hemiphot.R: Free R scripts to analyse hemispherical photographs for canopy openness, leaf area index and photosynthetic active radiation under forest canopies*. Unpublished report. Leiden, The Netherlands: Naturalis Biodiversity Center. URL: https://github.com/Naturalis/Hemiphot.

von Gadow, K. & G. Hui (2002). 'Characterising forest spatial structure and diversity'. In: *Proceedings of the IUFRO International workshop 'Sustainable forestry in temperate regions'*. Ed. by L. Bjoerk. Lund, Sweden, pp. 20–30.

Zhang, K., S.-C. Chen, D. Whitman, M.-L. Shyu, J. Yan & C. Zhang (2003). 'A progressive morphological filter for removing nonground measurements from airborne LiDAR data'. In: *IEEE Transactions on Geoscience and Remote Sensing* 41.4, pp. 872–882. DOI: 10.1109/tgrs.2003.810682.